Effect of the nature of both cation and anion substitution on the structural symmetry of Li-rich 3d-metal chalcogenide electrodes.

Jacques Louis[1,2], Clara Robert[2,3], Bernhard T. Leube[1,2], Anshuman Chaupatnaik[1,2], Neelam Sunariwal[4], Khagesh Kumar[4], Indrani Roy[4], Gwenaëlle Rousse[1,2,5], Jordi Cabana[4], Marie-Liesse Doublet[2,3] and Jean-Marie Tarascon[1,2]

Abstract:

Li-rich layered chalcogenides have recently led to a better understanding of the anionic redox process and its associated high capacity while providing ways to overcome its practical limitations of voltage fade and irreversibility. We first reported on the feasibility of triggering anionic activity in Li_2TiS_3, either through anionic substitution (Se for S) or cationic substitution (Fe for Ti). Herein, we further explore the chalcogenide chemical space to prepare mono-substituted $Li_{1.7}Ti_{0.85}Mn_{0.45}Ch_3$ (Ch = S, Se) and doubly substituted cationic and anionic phases ($Li_{1.7}Ti_{0.85}Fe_{0.45}S_{3-z}Se_z$) which crystallize either in the O3- or O1-type structures depending upon the nature of the substituents. All series show a bell-shape capacity variation as function of the transition metal (TM) substitution degree with values up to 240 mAh/g. For specific compositions, a structural O3 to O1 phase transition is observed upon Li removal, which is not reversible upon Li re-insertion due to kinetic limitations. DFT calculations confirm the O3 vs. O1 relative stability along the different series and point subtle electronic differences in the TM-doping, hence rationalizing the structural and electrochemical behaviors of these phases upon cycling. These findings provide further insights into the link between structural and electronic stability, which is of key importance for designing new chalcogenide-based anionic redox compounds.

Introduction

Lithium-rich layered oxides exhibit a high capacity as cathode materials due to the synergy of cationic and anionic redox processes[1]. This cumulative activity almost doubles the energy storage capacity of $Li_{1.2}Ni_{0.13}Mn_{0.54}Co_{0.13}O_2$ (Li-rich NMC) or cobalt-lean $Li_{1.2}Ni_{0.2}Mn_{0.6}O_2$ phases[2–4]. However, despite their excellent capacity, these materials suffer from limitations, including voltage fade, poor energy efficiency, and sluggish kinetics[5]. Significant progress has been made in elucidating the origin of the additional capacity, which is commonly attributed to the presence of oxygen non-bonding states near the Fermi level[6,7]. The participation of these states in the electrochemical activity of Li-rich transition metal oxides results in oxygen holes inducing the formation of either stable $(O_2)^{n-}$ dimers or unstable oxidized oxygen species, rising material-level problems such as cation migration, phase transition, and dioxygen formation. At the battery level, this oxygen oxidation introduces the aforementioned challenges, namely voltage fade, voltage hysteresis, and sluggish kinetics[5,8].

To meet these challenges, scientists have explored the anion-cation competition to design highly covalent systems. These systems feature enhanced stability of the oxidized anionic species due to the increased interaction between the anion *p* bands and the transition metal (TM) *d* bands. Initially, this strategy involved incorporating Co^{2+} as a substituent (e.g., $Li_{1.2}Ti_{0.6}Co_{0.2}S_2$)[9] to facilitate reversible anionic redox or preparing Ti^{3+}-substituted $Li_{1.33-y/3}Ti^{4+}_{0.67-2y/3}Ti^{3+}_yS_2$[10], inducing antisite occupation as observed in $NaCr^{3+}S_2$[11]. Furthermore, our research group demonstrated the feasibility of inducing anionic-redox activity in Li_2TiS_3 by introducing non-d^0 cations such as Fe^{2+} in $Li_{1.33-2y/3}Ti^{4+}_{0.67-y/3}Fe^{2+}_yS_2$[7], having a cationic $M^{2+/3+}$ redox band which is just positioned close to the S *3p* bands. Adjustment of anionic *p* levels by Se^{2-} doping into $Li_2TiS_{3-x}Se_x$ also proved effective[12]. In these sample series, some members achieved capacities of up to 270 mAh/g, while exhibiting reduced voltage fade, improved power rate capability, and enhanced energy efficiency compared to their oxide counterparts.

In our ongoing quest to increase the energy density of highly efficient Li-rich 3d-metal chalcogenides, we delve deeper into the design strategies offered by the rich chalcogenide chemistry. In this study, we explore new phases by investigating mono-substitutions of Ti for Mn in $Li_{2-2y/3}Ti_{1-y/3}Mn_yCh_3$ (Ch = S, Se), as well as dual-substitutions of Ti for Fe and S for Se, resulting in $Li_{1.7}Ti_{0.85}Fe_{0.45}S_{3-z}Se_z$ phases. We present the structural characteristics and electrochemical properties of these phases. In addition to their electrochemical activity, which is influenced by the degree of substitution, a noteworthy finding is that these layered phases

can crystallize in either O3 or O1 structures depending on the specific substitution scheme. The main structural difference in these two polymorphs is the connecting mode of the LiX_6 and TMX_6 octahedra that share edges in the former and faces in the latter. Interestingly, we also demonstrate that in certain systems, the O3 to O1 transition can be irreversibly triggered by the removal of Li. However, we show that this transition can be reversed by moderate thermal treatment showing that it is kinetically limited at room temperature. Density Functional Theory (DFT) calculations were used to elucidate the polymorph relative stabilities as a function of the Ti/TM and S/Se substitution degrees, and the Li-driven O3-O1 structural transition in order to identify indicators for predicting the stabilization of a targeted phase in either the O3 or O1 structure.

Results

Synthesis and structural characterization of pristine phases

Solid solutions $Li_{2-2y/3}Ti_{1-y/3}TM_yS_3$ and $Li_{2-2y/3}Ti_{1-y/3}TM_ySe_3$ ($0 \leq y \leq 0.75$; TM = Fe, Mn) were obtained by solid state methods by reacting stoichiometric amounts of thoroughly mixed precursors (Li_2S, TiS_2, Fe/Mn, S or Li_2Se, $TiSe_2$, Fe/Mn, Se respectively), assuming, in light of our previous studies[7], that both Fe and Mn ions adopt the +II oxidation state. As the aim of the study is to investigate Li-rich compounds, systems are studied up to y = 0.75 which is the limit of lithium enriched composition.

Figure 1 presents the XRD powder patterns for the $Li_{2-2y/3}Ti_{1-y/3}Mn_yS_3$ and $Li_{2-2y/3}Ti_{1-y/3}Mn_ySe_3$ ($y \leq 0.75$) series, along with the variation of the lattice parameters as a function of the degree of substitution. Regardless of the S or Se series, all the synthesized materials crystallize in a rhombohedral space group $R\bar{3}m$, also known as O3[13], similar to undoped Li_2TiS_3 and Li_2TiSe_3. Rietveld refinements (see Supplementary Information Tables S1-4) do not indicate the presence of transition metals within the Van der Waals alkali layers. The continuous [illegible]ease in lattice parameters *a* and *c* with TM content suggests the presence of solid solutions up to y = 0.75 and y = 0.6 for the sulfides and selenides series, respectively. [illegible]tiple attempts, varying the temperature from 400°C to 850°C, dwelling time from 12h to 72h, or grinding the sample

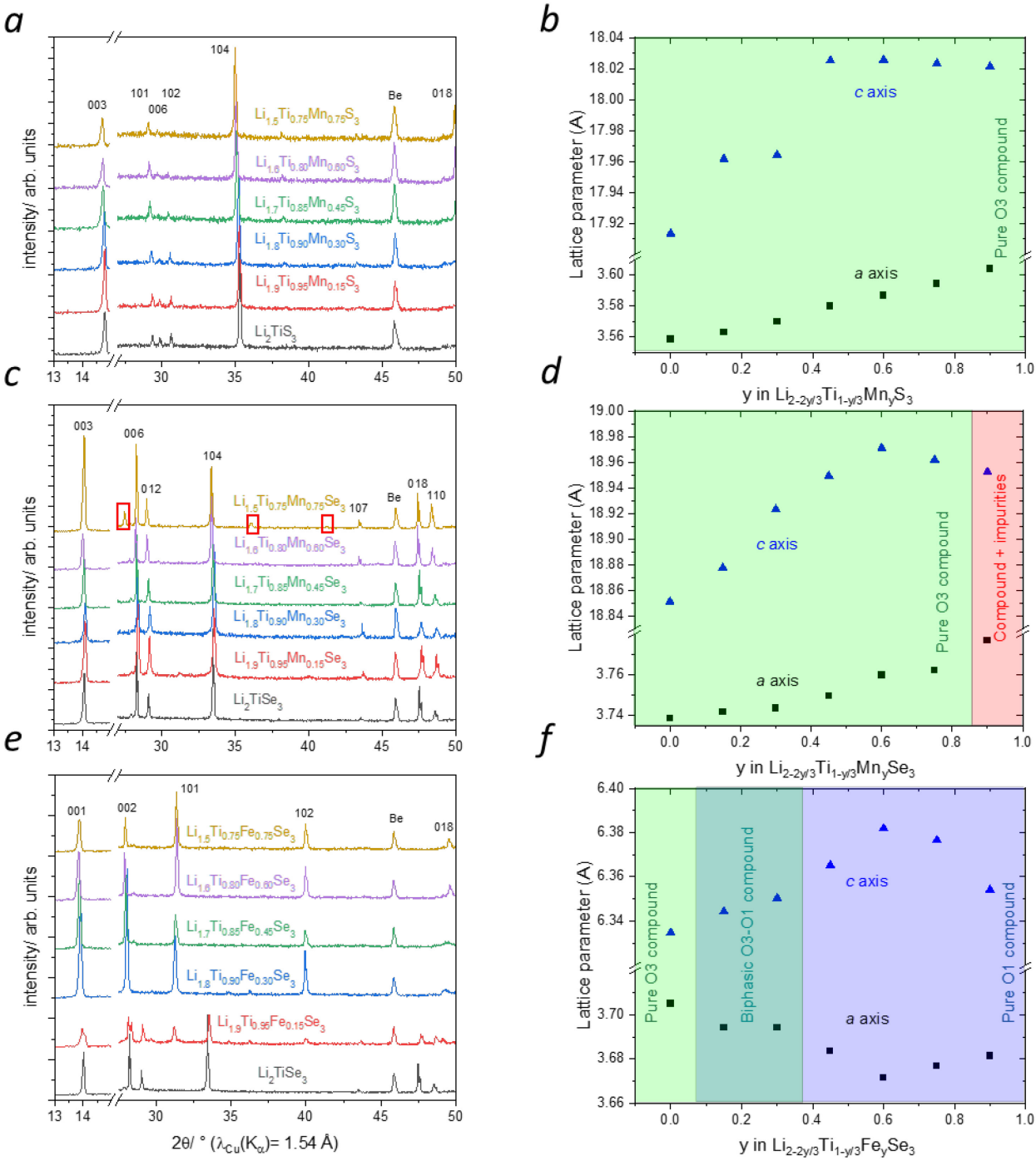

Figure 1: *PXRD pattern of synthesized materials in Mn-substituted Li_2TiS_3 (**a**), Mn-substituted Li_2TiSe_3 (**c**), and Fe-substituted Li_2TiSe_3 (**e**) series. Lattice parameters refined in $R\bar{3}m$ (O3) or in $P\bar{3}m1$ (O1) plotted against the substitution ratio y in $Li_{2-2y/3}Ti_{1-y/3}Mn_yS_3$ (**b**), $Li_{2-2y/3}Ti_{1-y/3}Mn_ySe_3$ (**d**), and $Li_{2-2y/3}Ti_{1-y/3}Fe_ySe_3$ (**f**). In **e**, the relative peak intensity 001/101 shift between $Li_{1.7}Ti_{0.85}Fe_{0.45}Se_3$ and higher Fe ratio compounds, is taken into account through lower preferential orientation. In **f**, the c lattice parameter of O3-Li_2TiSe_3 is divided by 3 to compared with the Fe-doped O1 counterparts. Only the O1 lattice parameters are reported in the biphasic domain.*

between two heat treatments, were tried for the synthesis of $Li_{1.5}Ti_{0.75}Mn_{0.75}Se_3$, all leading to XRD patterns with extra peaks beyond those attributed to the O3 phase, indicating the presence of impurities (see Figure 1, red rectangles). It should be noted that our efforts to stabilize the

"$Li_2Ti_{0.7}Mn_{0.3}S_3$" and "$Li_2Ti_{0.7}Mn_{0.3}Se_3$" compositions with Mn in the +IV oxidation state resulted in multiphase samples, with the Mn^{2+}-doped compound being the main phase coexisting with Li_2S(Se) and Mn-based impurities (see Supplementary Information Figure S1).

For the Fe-doped $Li_{2-2y/3}Ti_{1-y/3}Fe_ySe_3$ series a solid solution domain up to y = 0.75 was obtained, but it enlists a phase change from O3 (space group $R\bar{3}m$) to O1 (space group $P\bar{3}m1$) that occurs over the composition range (y = 0.15-0.3). Afterwards, the O1 phase becomes the sole component and shows a continuous increase of the d decrease of the *a* lattice parameters up to y = 0.6, followed by an inversion of the linear trend thereafter (see Figure 1). This contrasts with the predominance of the O3-type structure for the Fe-doped sulfide[7], Mn-doped sulfide and Mn-doped selenide series and suggests a delicate balance in the degree of cation-anion substitution as the origin of the polymorphism stability.

ighlight the importance of synthesis conditions on the appearance of the O1 phase in this series, we checked the effect of the partial pressure during synthesis. By changing the total volume of the ampule for the same amount of reagents, we note that a lower Se pressure promotes the O1 polymorph (see Supplementary Information Figure S2).

To complement this study, we investigated the dual cation-anion substitution space by exploring the complete $Li_{1.7}Ti_{0.85}Fe_{0.45}S_{3-z}Se_z$ domain from O3-$Li_{1.7}Ti_{0.85}Fe_{0.45}S_3$ (z = 0) to O1-$Li_{1.7}Ti_{0.85}Fe_{0.45}Se_3$ (z = 3). Our results show that the O3 to O1 transition occurs around z = 1.5 with, however, the co-existence of both the O3 and O1 polymorphs in the range $1.5 < z < 2.5$ (see plementary Information Figure S3). It should be noted that same end-products were obtained when the synthesis was carried out with the appropriate mixture of $Li_{1.7}Ti_{0.85}Fe_{0.45}S_3$ and $Li_{1.7}Ti_{0.85}Fe_{0.45}Se_3$ (see Supplementary Information Figure S4).

Electrochemical cycling

To check the influence of polymorphism on the electrochemical performance of the synthesized materials, Li-half Swagelok cells were assembled using members of different series as positive electrodes. The cells were cycled between 1.8 and 3.2 V at C/20, and the collected data is shown in Figure a function of the Li content for each series.

Although undoped Li_2TiS_3 and Li_2TiSe_3 electrodes show poor activity, TM-doped electrodes show notable electrochemical performances irrespective of the transition metal (Fe, Mn). For all series, the voltage-composition curves exhibit a relatively well-defined potential plateau

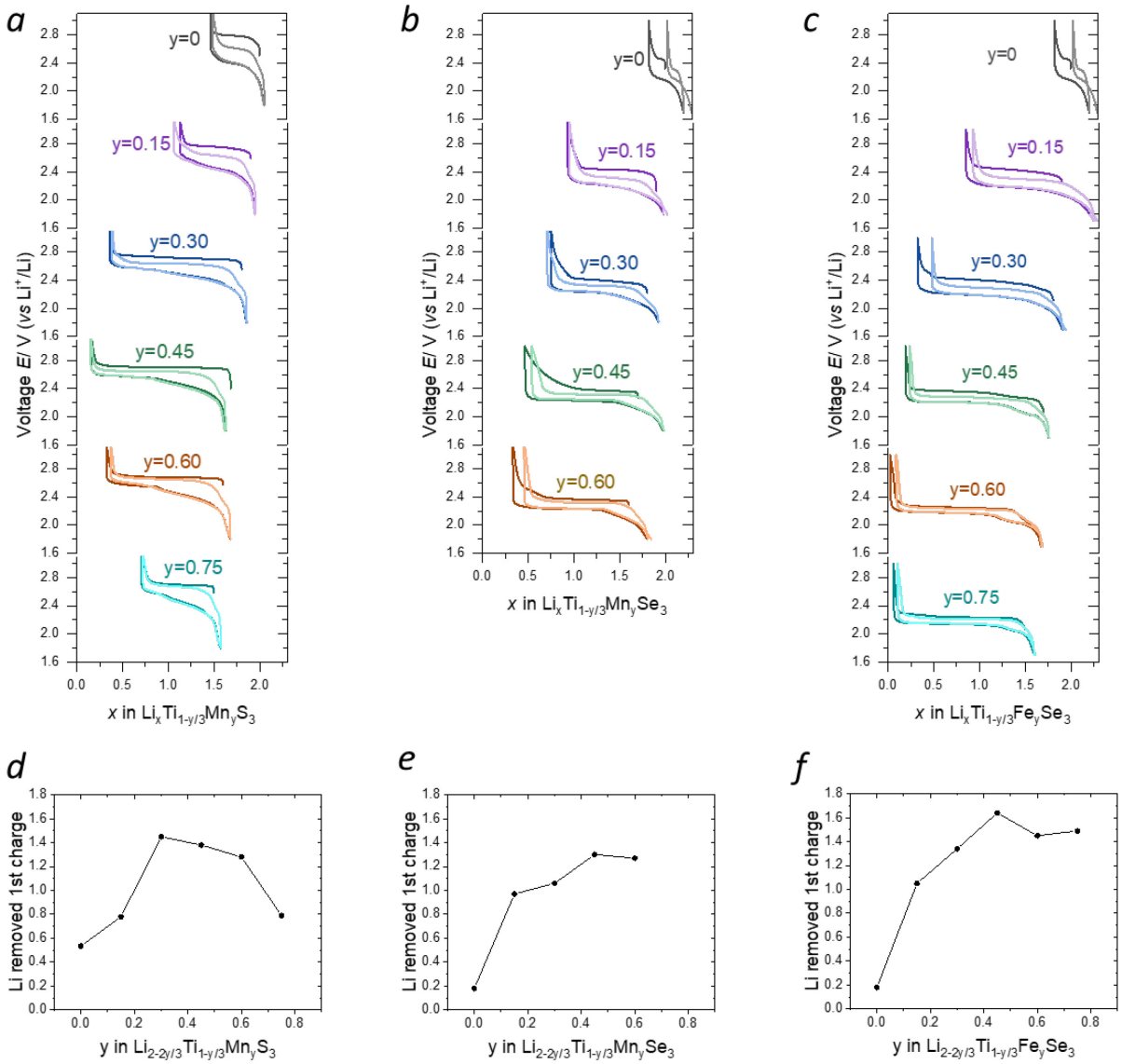

***Figure 2**: Voltage profiles of the first (darker color) and second (light color) cycles for the different substituted series (**a**, **b**, **c**). (**d**, **e**, **f**) show the experimental first charge Li removal (black) as a function of the substitution ratio y compared to the theoretical possible Li removal from cationic redox associated with either the TM^{2+}/TM^{3+} (blue) or TM^{2+}/TM^{4+} (purple) redox couples.*

during charge, indicating a two-phase process (see Supplementary Information Figure S5). The Fe-doped selenide series displays the lowest polarization in the voltage-composition profile, particularly for the pristine O1 phases obtained at high TM substitution (y > 0.3). This behavior is very similar to the one of the previously reported Fe-doped sulfide series, except that the sulfides are O3 (from Sah). During discharge, two distinct redox processes can be observed, with relative amplitudes depending on the *y* ratio. For Mn-doped sulfides, the second process occurs over a wider range of Li-composition than in the corresponding selenides and is always more polarized than the first process in all cases.

arkably, the number of Li exchanged during the first charge of all series does not increase linearly with the amount of TM but displays a bell-shaped behavior with a maximum reached around y = 0.3 for the Mn-doped sulfides; and a rapid increase with a maximum at y = 0.45 followed by a stagnation / low decrease for the Mn- and Fe-doped selenides. The total capacity of the electrodes is greater than the theoretical capacity expected from a pure cationic redox (depicted for TM^{2+}/TM^{3+} or TM^{2+}/TM^{4+} redox couples in Supplementary Information Figure S6), suggesting cumulative cationic and anionic electrochemical activity in these systems.

The compounds with y = 0.45 of the different systems were then considered as representative of their series for deeper characterization. To confirm the role of the chalcogens, X-Ray Absorption Near Edge Structure (XANES) measurements were conducted at 5 different states of charge (see Supplementary Information Figure S7-S8) for both $Ti_{0.85}Mn_{0.45}Ch_3$ (Ch = Se, S). The K-edge data confirm the pristine oxidation states Ti^{4+}, Mn^{2+}, S^{2-} and Se^{2-} as designed. ates below 2472 eV (see Figure 3a) arise from transitions to hybridized S 3p-Mn 3d states and their splitting reflects the crystal field strength in the octahedral environment. The absorption edge involves higher transitions and is dominated by the photoionization threshold, which provides a convenient way to probe changes in Z_{eff}. The most visible changes upon charging and discharging are a reversible change in the intensity and position of the pre-edge peak at 2468.5eV and in the position of the absorption edge above 2472 eV, both of which have

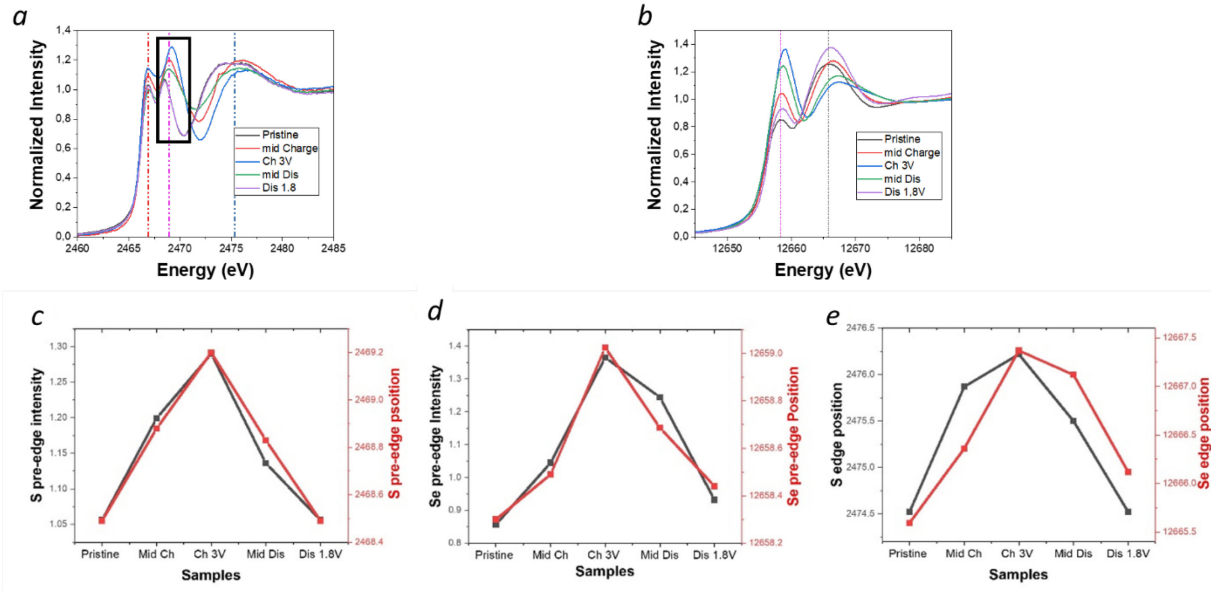

***Figure 3**: XANES measurement of S K-states in $Li_{1.7}Ti_{0.85}Mn_{0.45}S3$ (**a**) and of Se K-states in $Li_{1.7}Ti_{0.85}Mn_{0.45}Se_3$ (**b**). The second pre-edge pic of S, corresponding to an hybrid Ti-Mn-S state (squared in (**a**)), follows a position and intensity bell-shape along cycling (**c**). Same bell-shape behavior is displayed by Se K pre-edge (**d**) and S and Se edges (**e**). The implication of the chalcogen is thus emphasized in the redox process of the Mn-doped series.*

been reported to track the participation of the S states in a reversible redox ess (see Figure 3c and e)[14–16]. The same general observations were made for the Se K pre-edge and edge (below and above 12663 eV, respectively, in Figure 3b, d and e). oth series, there is only a slight shift of the Mn K and L-edge XAS, suggesting oxidation to an intermediate oxidation state between +II and +III (see Supplementary Information Figure S7-S8 e and S9)[17]. Therefore, TM but largely Ch, are responsible for the electrochemical activity of the studied compounds.

The Fe-doped selenide series displays the lowest polarization, particularly for the pure O1 phase obtained at high TM substitution (y > 0.3). Strikingly, for low Fe substitution Strikingly, for low Fe substitution the first discharge capacity is higher than the first charge capacity. Such additional Li insertion is also observed in the O3 Mn-doped Se series, but for the higher y ratios, and to a lesser extent in the Mn-doped S series. Irrespective of the nature of O3 or O1 polymorph (see Supplementary Information Figure S2), this indicates material oxidation, most likely due to Li and/or TM vacancies in the pristine phases.

nterrogate the influence of chalcogen on the additional Li capacity, the samples of the $Li_{1.7}Ti_{0.85}Fe_{0.45}S_{3-z}Se_z$ series (z = 0 to 3) were also cycled in Li-half cells, following the same procedure as for the other series (see Supplementary Information Figure S3). The first two galvanostatic cycles of this series show that the extra-capacity observed on discharge tends to decrease after the first cycle, e the members of the pure selenide series, confirming that this extra-capacity is due to a pristine state slightly oxidized.

Structural behavior upon cycling

We now focus on the structural transformation that occurs during charging and discharging the mono- and dually-substituted TM-X series (Mn-S, Mn-Se, Fe-Se and Fe-SSe). We first discuss $Li_{1.7}Ti_{0.85}Fe_{0.45}Se_3$, whose phase purity was confirmed by both Neutron Powder Diffraction (NPD) and Synchrotron X-Ray Diffraction (SXRD) (see Supplementary Information Figure S10). This phase shows a capacity of 140 mAh/g, lower than its sulfide counterpart O3-$Li_{1.7}Ti_{0.85}Fe_{0.45}S_3$ (250 mAh/g), due to the difference between the molar masses of S and Se[7]. The structural mechanism of O1-$Li_{1.7}Ti_{0.85}Fe_{0.45}Se_3$ was examined by *in situ* X-ray diffraction (see Figure 4). As the cell is charged, a progressive disappearance of some peaks gives way to new ones that sharpen to give a well-defined XRD powder pattern for the fully de-lithiated state. The new peaks could be fully indexed in an O1-type structure with lattice parameters *a*=3.48582(15) and *c*=6.08799(40) Å, as determined separately by SXRD. This implies a two-

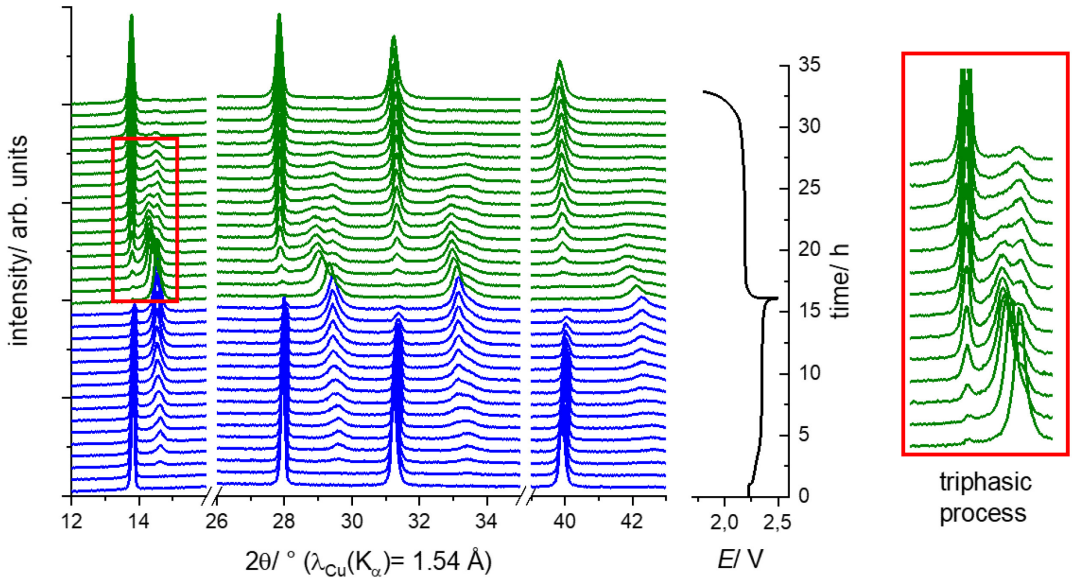

***Figure 4**: Operando in situ PXRD of O1-$Li_{1.7}Ti_{0.85}Fe_{0.45}Se_3$ upon first galvanostatic cycle. The first charge shows a biphasic domain while the first discharge is composed of a solid solution with a triphasic system, completed by a biphasic system back to the pristine material pattern.*

phase de-intercalation process between two O1-type structures having different volumes. Subsequent discharge reveals a more complex reaction pathway that ultimately converts back to the O1 pristine material: the fully charged phase is first converted through a concomitant solid solution and biphasic process at the beginning of discharge, while only a biphasic domain is observed at the end of discharge. The solid solution domain does not extend from the charged phase to the discharged phase but it is visible up to an intermediate phase, which is then converted by a biphasic process in the discharged phase, close to the pristine one. three-phase system is certainly due to a particle size distribution, which allows larger grains to maintain the charged phase because of Li diffusion while the smaller ones are rapidly converted to the discharged phases.

Similar *in situ* XRD studies were conducted for a sulfide and selenide with the same Mn content, namely O3-$Li_{1.7}Ti_{0.85}Mn_{0.45}S_3$ and O3-$Li_{1.7}Ti_{0.85}Mn_{0.45}Se_3$ (see Figure 5). Remarkably, upon charging, the selenide undergoes a structural transition to the O1 phase, which persists through subsequent cycles, rather than reconverting to O3 on discharging. In contrast, the sulfide sample preserves the O3-type stacking during the first charge and discharge cycles, like $Li_{1.7}Ti_{0.85}Fe_{0.45}S_3$.[7] Interestingly, the peaks of the growing phase slightly shift towards higher angles suggesting a solid solution behavior in the second part of the charge. XANES measurements support the existence of the irreversibility of the Mn-doped selenide, since both the Se K and Mn K spectra return less closer to the pristine state than in the case of S and Mn

in the sulfide (see Figure 3 and Supplementary Information Figure S8-S9). Moreover, the Ti K and L-edge XAS [illegible]e that the latter corresponds to near-surface signals because measurements with bulk detection were excessively noisy), whose fine structure is very sensitive to the local environment, also points at a change in local symmetry in the charged state of the selenide, whereas it is quite stable in the sulfide (see Supplementary Information Figures S8-S9).

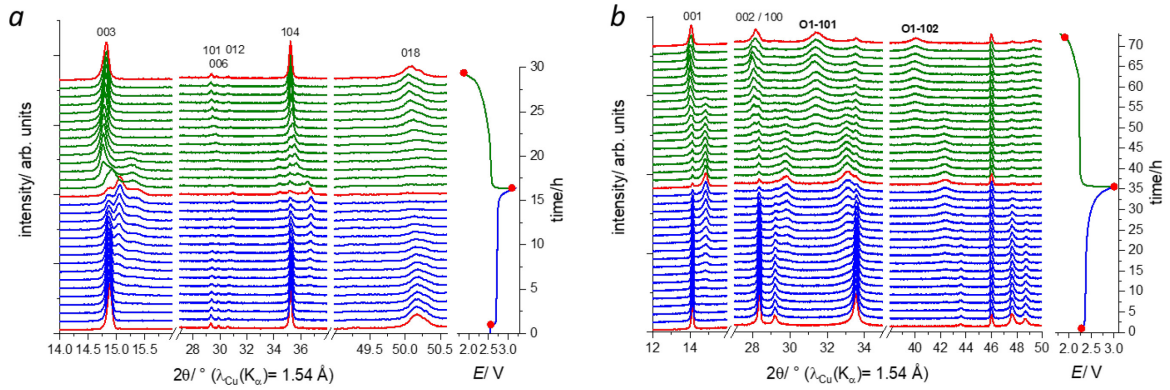

***Figure 5**: Evolution of the in situ XRD patterns in the first cycle of **(a)** $Li_{1.7}Ti_{0.85}Mn_{0.45}S_3$/Li and **(b)** $Li_{1.7}Ti_{0.85}Mn_{0.45}Se_3$/Li half-cells at a rate of C/10 and C/20 rate, respectively. XRD patterns were collected for every change in lithium stoichiometry of 0.1 of the sulfide series and 0.05 for the selenide series.*

To confirm the persistence of the O3 phases for the Mn and Fe-doped sulfides, *ex situ* XRD patterns were collected on the samples after 5 cycles. [illegible]oped sulfide $Li_{1.7}Ti_{0.85}Fe_{0.45}S_3$ shows partial conversion to an O1 stacking while the Mn-doped sulfide is fully O3, even after [illegible] cycles (see Supplementary Information Figure S11). Unlike the $Li_{1.7}Ti_{0.85}Fe_{0.45}S_3$ end-member, all cycled materials in the dually substituted system fully transitioned to the O1 phase after 5 cycles (see Supplementary Information Figure S12). Interestingly, an annealing procedure at 150°C and 250°C is sufficient to convert cycled O1-$Li_{1.7}Ti_{0.85}Fe_{0.45}S_{2.5}Se_{0.5}$ and O1-$Li_{1.7}Ti_{0.85}Mn_{0.45}Se_3$ back to an O3 stacking, respectively (see Figure 6). All these results confirm that Fe-doped compounds favor the O1 phase more than their Mn-doped counterparts (whether after cycling for the sulfides, or even directly in the pristine state for the selenides or sulfides/selenides) and that the reverse O1 to O3 transition in discharge is kinetically limited.

At this stage, in addition to modifying the host structure by cationic or anionic substitution, we explored the effect of the guest alkali ion on the onset of the O3 to O1 phase transition, by replacing Li^+ with Na^+. To this end, O3-$Li_{1.7}Ti_{0.85}Mn_{0.45}Se_3$ was electrochemically oxidized up to 3 V in a Li-based cell to produce the delithiated O1-$Li_{0.6}Ti_{0.85}Mn_{0.45}Se_3$, before being used

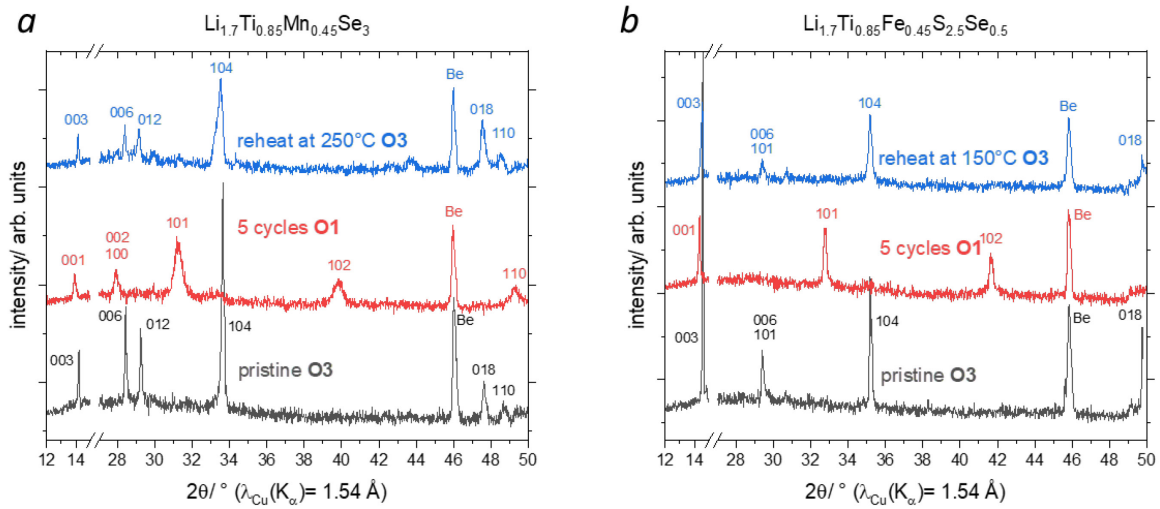

Figure 6: *PXRD of pristine, after 5 cycles, and after heat treatment of $Li_{1.7}Ti_{0.85}Mn_{0.45}Se_3$ **(a)** and $Li_{1.7}Ti_{0.85}Fe_{0.45}S_{2.5}Se_{0.5}$ **(b)**. Both compounds undergo the O3 to O1 transition upon cycling, while a heat treatment with moderate temperatures (250°c and 150°C, respectively) allows the recover of the O3-type structure.*

as positive electrode in fresh Na half-cell. The cell voltage profile (see ure 7) shows the presence of single redox plateaus on discharge and charge indicating that the O1 phase can reversibly absorb 1.3 Na^+ via a two-phase process. The strong polarization between the charge and discharge and the overshoot voltage at the start of discharge is indicative of a kinetically limited Na^+ uptake and removal process. Its biphasic nature was confirmed by operando XRD measurements, with polymorph O1 disappearing at the expense of polymorph O3 during discharge and the reverse during charge. This contrasts sharply with the irreversible transformation of O3 into O1 during charging in Li-ion cells. This observation suggests that the d-spacing is a key metric governing the O3-O1 phase transition.

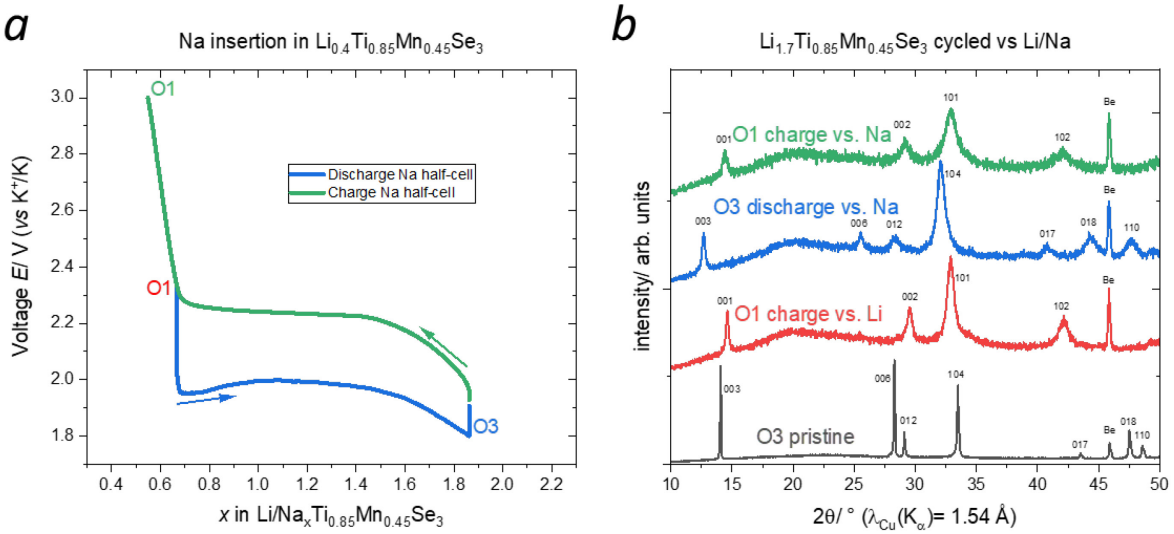

Figure 7: *Reversible electrochemical insertion of Na in charged O1-$Li_{0.6}Ti_{0.85}Mn_{0.45}Se_3$ **(a)**. PXRD of the Mn-doped selenide at different states of charge in Li-ion or Na-ion cells **(b)**. Compared with Li cycling, Na allows a reversible phase transition from O1-charged phase to an O3-discharged phase.*

Discussion

We have reported the possibility of triggering anionic redox activity in Li_2TiS_3-type frameworks sulfides via partial substitution of Ti for Fe or Mn, and the partial or total substitution of S for Se (see Figure 2 and Supplementary Information Figure S3). The resulting solid solutions crystallize in either a O3-type or O1-type structure and feature electrochemical capacities as high as 240 mAh/g as well as low polarization (~100 mV) compared to oxides (400-500 mV). In addition to the complexity of the Li uptake-removal, which can involve cumulative cationic and anionic redox processes depending on the nature of the cation and anion, a Li-driven O3 to O1 structural transition was observed during charging, mainly for the Se and Fe-rich compounds. Surprisingly, the O3 to O1 transition is not reversible upon discharge, unless thermal annealing is applied or Na^+ ions are inserted in the electrochemically de-lithiated O1 electrodes (see Figure 6 and Figure 7). The compositions and structural type for the pristine and electrochemically cycled materials are summarized in Figure 8

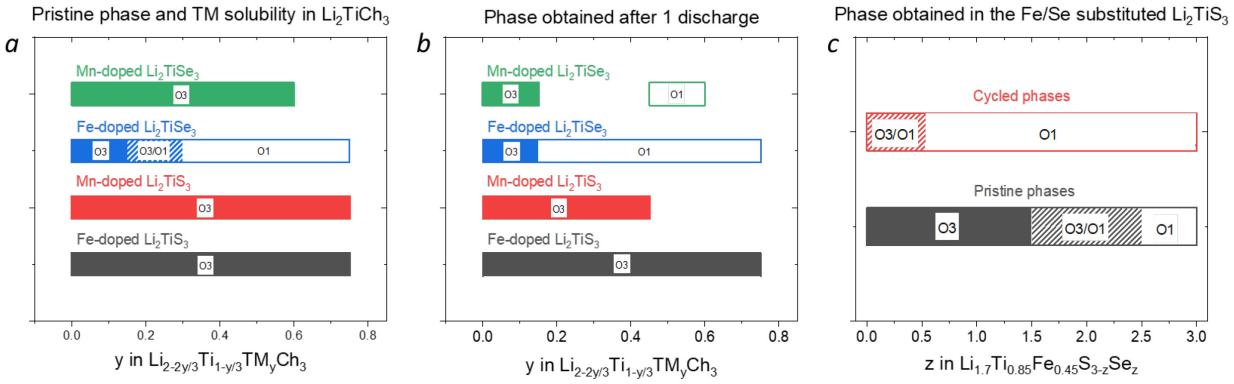

Figure 8: *Phases of the Fe-doped and Mn-doped Li_2TiCh_3 (Ch = S, Se) at the pristine state (a) or after 1 cycle (b). Phases of the Fe/Se-doped Li_2TiS_3 series at pristine and cycled state (c). Only some of the compounds were recover for XRD analysis after cycling, explaining the difference in composition data between (a) and (b).*

Early studies have highlighted the critical role of covalency in the stabilization of the O1 over O3 polymorph[18]. Accordingly, the increase in system covalence through the chemical substitution of S by the larger, less electronegative chalcogen Se naturally favours the O1-type structure in the Se-rich series of TM-doped pristine materials. Similarly, the increase in covalency typically associated with electrochemical oxidation of cations or anions (or both) may explain the Li-driven O3 to O1 transition observed during oxidation for some of the electrodes in this study. However, this hand-waving rules do not explain why Se-rich phases such as the Li-rich Li_2TiSe_3 exist in the O3-type structure, why Fe doping is more favourable to the O1 stacking than Mn, and why the O3 to O1 transition upon charge is not reversible upon

discharge with Li as the ion carrier. These apparent contradictions stem from the fact that covalence is a multiparametric quantity arising from a subtle balance between orbital overlaps (directly or indirectly linked to properties such as electronegativity, electronic structure and local symmetry) and electrostatic (linked to oxidation states and structural environment). This motivated us to rationalize experimental facts by DFT calculations with the aim of establishing links between the chemical composition of the undoped and TM-doped materials and their structural, electronic and electrochemical properties.

Rationalizing the O1- vs O3-type structures in pristine materials

Spin-polarized DFT calculations were performed on the sulfides and selenides series of undoped, Fe-doped and Mn-doped Li_2TiCh_3 materials (Ch = S, Se), both in the O3- and O1-type model structures with 36 chalcogen atoms per supercell. Undoped $Li[Li_xTi_{1-x}]Ch_2$ phases were used as reference systems to rationalize the role of TM-doping on the structural and electrochemical properties of the electrodes. Since x controls the average transition metal charge, the Ti/TM ratio was systematically adapted so as to keep the formal TM^{2+} oxidation state in the Fe- and Mn-doped materials (close to the experimental benchmark). For all TM-doped materials, different Li/Ti/TM (TM = Fe, Mn) cationic distributions were considered before investigating delithiation (see Supplementary Information Figure S13).

In agreement with the experimental XRD observations, theoretical predictions confirm that Fe- and Mn-doping lead to cationic disorder in the honeycomb layer at room temperature, since all the cationic distributions considered in the calculations differ in energy by no more than the thermal activation energy at 300 K (see Supplementary Information Figure S13). For each doping element (TM = Fe or Mn), the O3 and O1 polymorphs display very close electronic structures and energies, thus making their discrimination from simple thermodynamic considerations not so straightforward. Nevertheless, as depicted in Supplementary Information Figure S14, the relative energies of the O3 and O1 polymorphs ($\Delta E_{O3\text{-}O1}$) for the undoped and TM-doped materials, calculated for different Ch/TM ratios, reproduces the correct experimental trends. It confirms that (i) the chemical substitution of S for the less electronegative Se anion invariably favours the O1 polymorph ($\Delta E_{O3\text{-}O1} > 0$ or less negative) irrespective of the TM-doping and (ii) the chemical substitution of Ti for more correlated Fe and Mn transition metals invariably favours the O3 polymorph ($\Delta E_{O3\text{-}O1} < 0$ or less positive)[19]. The evolution of $\Delta E_{O3\text{-}O1}$ also reveals that Li-rich $Li_2TM^{4+}Ch_3$ systems ($x = 0.33$) favor the O3-type structure over their "Li-poor" $LiTM^{3+}Ch_2$ analogues ($x = 0$), despite the increase in TM-Ch covalency associated

with the increase of the TM oxidation state. This means that electrostatic interactions are also critical in the O3 vs. O1 polymorph stability, in particular the interlayer cation-cation repulsions ($M^{n+} – Li^{+} – M^{n+}$) which favour the O3 polymorph when moving from $LiTMCh_2$ to Li_2TMCh_3. Accordingly, covalence can be considered as the correct descriptor predicting the relative stability of O1 and O3 polymorphs only when comparing materials with equivalent Ch/TM stoichiometries (i.e. equivalent TM oxidation states), since in this case, covalence and electrostatics contribute in the same direction to the preference of O1 over O3.

Rationalizing the preference of O1 vs. O3 polymorphs induced by electrochemistry

The amount of intercalated Li adds another dimension which complicates the study. Following the same reasoning as above, the electrochemical oxidation (Li extraction) is expected to eliminate (at least partially) the interlayer $M^{n+} – Li^{+} – M^{n+}$ electrostatic repulsions and to concomitantly increase the covalence of the system due to the oxidation of the cations and/or anions, therefore favouring the O3 to O1 transition during charging. Focussing on the relative energy of O3 vs. O1, DFT (T = 0 K) phase stability diagrams were computed in the whole range of Li composition between the pristine (x = 1.667) and charged (x = 0.1667) materials for the four TM-doped sulfides and selenides series. As depicted on Figure 9, the thermodynamic preference of the O1 polymorph is confirmed for the Fe-rich and Se-rich materials with, however, no clear discrimination between the two polymorphs for the sulfides series for which both O1 and O3 are within the room-temperature thermal energy, irrespective of the Li content. This suggests that the O1 preference is more related to the chalcogen nature than to the delithiation degree and that subtle electronic and/or kinetic factors govern the O3 to O1 transition. Despite the possibility of preparing a wide range of layered phases, the search for an unambiguous explanation of the O3 to O1 phase transition remains complex due to specific differences for each series, especially considering the different behavior when Na^{+} instead of Li^{+} is used as the guest ion. Na insertion shows a reversible O1-O3 transition, implying a thermodynamically controlled process. In contrasts, Li-based compounds all show the O3 to O1 transition through a biphasic process on charging which again is thermodynamically controlled, but the transition back to O3 is somehow more difficult to achieve, probably due to the solid solution behavior of Li insertion at the beginning of discharge. This suggests a kinetically controlled discharge mechanism on the Li-cells and possible reasons for such a difference between Li^{+} and Na^{+} insertion process could be rooted in an easier Na^{+} ion diffusion associated with a lower energy barrier consistent with a larger d-spacing. This is initially

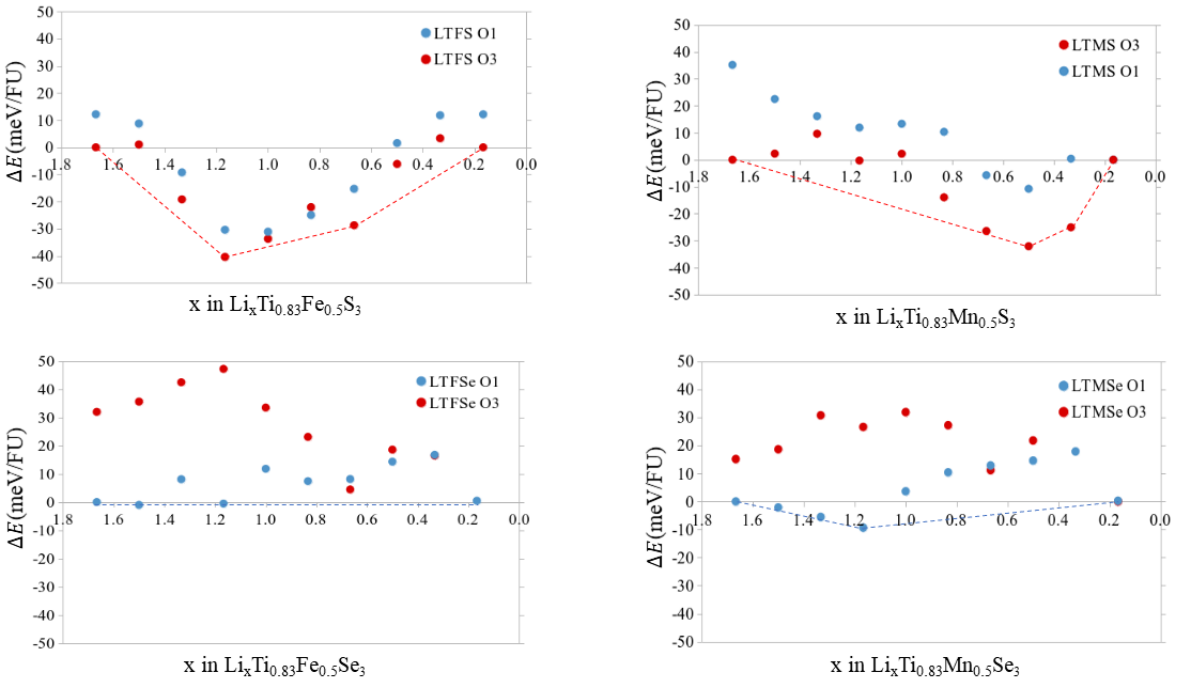

***Figure 9**: Phase stability diagrams computed in the whole range of Li composition of the $Li_xTi_{0.833}TM_{0.5}Ch_3$ electrodes (TM=Fe, Mn ; Ch=S, Se) computed with DFT+U with respect to the most stable pristine and delithiated end-members. The dotted lines represent the convex hull of each phase stability diagram, i.e. the electrochemical processes expected during delithiation/lithiation at thermodynamic equilibrium, considering that the thermal activation energy is k_BT = 25meV at room temperature. All pristine and delithiated phases are predicted in the same structure as the experimental ones, except for the $Li_{1.667}Ti_{0.83}Mn_{0.5}S_3$ pristine phase which is found slightly more stable in O1 than in O3 by less than k_BT, probably due to the slightly higher Mn stoichiometry used in the calculations compared to experiments.*

counter-intuitive since the polarization for the Na insertion process is comparable to that of Li insertion but it must be recalled that a large energy gap can exist with fast kinetics.

Conclusion

In this paper, we have shown the richness of the Li-rich layered chalcogenide chemistry that offers many possibilities via cationic and anionic substitutions to adjust band positioning and trigger anionic redox. This exploration leads to multitude compounds having energy densities as high as 240 mAh/g while showing nearly zero irreversible capacity during cycling and a voltage polarisation lower than the corresponding oxides. However, the complexity of these materials stems from their polymorphism, as they can exist in either the O3 or O1 structure, depending on the nature of the cationic-anionic substituents and the Li concentration. Finding reliable indicators to predict the stability of one polymorph over the other is complex due to the small energy difference between the two polymorphs, as confirmed by DFT. While the O1 vs. O3 thermodynamic stability is very similar, the irreversible O3 to O1 transition observed upon

charging is likely due to kinetic limitations in discharge, as suggested by the O1 to O3 reverse reaction evidenced during low temperature heat treatment, or re-insertion of Na^+ rather than Li^+ to increase the interlayer d-spacing. Further work is needed to specifically address this question and provide guidance for enlarging this class of high-capacity Li-rich layered chalcogenides, which is of great interest for the development of solid-state batteries based on sulfide ionic conductors, thus bypassing detrimental interfacial issues.

Methods

Synthesis method: The different series compounds were synthesized by mixing in an argon (Ar)-filled glovebox, lithium sulfide (Alfa-Aesar, 99.9%), titanium sulfide (Sigma-Aldrich, 99.9%), iron powder (Sigma-Aldrich, 99%), manganese powder (Sigma-Aldrich, 99%), elemental sulfur (Sigma-Aldrich, 99.998%) and elemental selenium (Alfa Aesar, 99.999%) in stoichiometric amount. The powder was then ground in an agate mortar for 10min, prior to be transferred in a quartz ampule subsequently sealed under vacuum ($<10^{-3}$ mbar). The resulting ampule was then placed in an oven at 750°C for 48h with a heating rate of 1°C/min and natural cooling after furnace was turned off at the end of dwelling time. The powder was collected in Ar-filled glovebox and stored as such.
Delithiated phase were obtained after electrochemical delithiation and recover from half-cells, washed 3 times with dimethyl carbonate (DMC), and dried under primary vacuum before further use.

Electrochemical Measurements: Swagelok-type cells were assembled in an Ar-filled glovebox using positive electrodes made by ball-milling (SPEX Mixer/Mill 8000M) in 45mL stainless steel jar with one 8mm stainless steel ball, the active materials synthesized with 20% in mass carbon Super P (Alfa-Aesar, 99+%). Lithium metal or sodium metal are used as the negative electrode. Both electrodes were separated by a Whatmann GF/D borosilicate glass fibers sheets cut to an appropriate size and soaked in LP30 electrolyte (1 M LiPF6 in a mixture of EC/DMC 1:1 by volume), or in 1.0 M $NaPF_6$ in EC/DMC (50%/50% by volume). The cells were then cycled in a Biologic galvanostat/potentiostat (MPG-2/ VMP-3) using galvanostatic (constant current) mode.

X-ray Diffraction: Synchrotron X-ray powder diffraction (SXRD) patterns were measured at the 11-BM beamline of the Advanced Photon Source (Argonne National Laboratory) with λ = 0.45789 Å. To limit absorption, the powders were mixed with dried amorphous silica in an Ar-filled glovebox and sealed in glass capillaries of 0.6 mm diameter. X-ray powder diffraction and *Operando* powder X-ray diffraction (XRD) experiments were performed in an airtight electrochemical cell equipped with a Be window, assembled in an Ar-filled glovebox. The patterns were then collected in Bragg−Brentano geometry using a Bruker D8 Advance diffractometer equipped with a Cu K_α X-ray source (λ_1 = 1.5406 Å, λ_2 = 1.5444 Å) and a LynxEye XE detector. Finally, the refinement of the diffraction patterns was done following the Rietveld method using the FullProf program.

Neutron Powder Diffraction: A constant wavelength neutron powder diffraction (NPD) pattern of approximately 1.5 g of pristine $Li_{1.7}Ti_{0.85}Fe_{0.45}Se_3$ was recorded on the Echidna diffractometer, ANSTO (Australian Nuclear Science and Technology Organization).

X-Ray Absorption Near Edge Structure (XANES): Mn, Ti $L_{II,III}$-edge XAS measurements were carried out at beamline 29-ID at the Advanced Photon Source, Argonne National Laboratory. Ti L-edge and Mn L-edge spectra were collected in TEY and TFY modes at room temperature and under ultra-high-vacuum conditions (below 10−8 torr). Contributions from visible light were carefully minimized before the acquisition, and all spectra were normalized by the current from freshly evaporated gold on a fine grid positioned upstream of the main chamber. The measured spectra were aligned using beamline reference and a basic normalization using a linear background. S, Se K-edge, Ti K and Mn K XAS experiments were performed at the beamlines 9-BM-B, 5-BM-D and 10-ID-B respectively, at the Advanced Photon Source, Argonne National Laboratory. XAS spectra were collected in fluorescence mode using an ion chamber (Mn K) and 4-element silicon drift detectors (Ti K, S K). The incident beam was monochromatized by a Si (111) fixed-exit double-crystal monochromator. A metal reference foil was measured simultaneously with each sample for energy calibration at Ti K and Mn K, while for calibration at S K sodium thiosulfate standard was ran before and after the measurement. Data analysis was completed using the IFEFFIT package[20].

Computational details DFT: Spin-polarized density functional theory (DFT) calculations as implemented in VASP (Vienna ab initio simulation package)[21,22] were performed, using the projected

augmented wave method (PAW)[23]. The generalized gradient approximation of Perdew−Burke−Ernzerhof (PBE)[24] in conjunction with the rotationally invariant Dudarev method (DFT+U)[25] to treat the d-electrons. As a consequence of the relatively strong covalence of the Ti-S and Ti-Se bonds, the self-interaction error is limited in these systems thanks to the efficient screened of the on-site coulombic repulsions by the long-range electron delocalization over the structure. As a consequence, DFT+U with moderate U_{eff}(Ti) = 0 or 2eV and U_{eff}(Mn, Fe) = 2 or 4 eV lead to similar results.

Acknowlegments

The authors warmly acknowledge M. Avdeev for performing NPD diffraction experiments on the Echidna diffractometer, Australian Nuclear Science and Technology Organization (ANSTO). This work used the 11-BM mail service and XAS beamlines 9-BM, 5-BM, 29-ID, and 10-ID of the APS, a US Department of Energy (DOE) Office of Science User Facility operated for the DOE Office of Science by Argonne National Laboratory under contract no. DE-AC02-06CH11357. N.S., K.K., I.R. and J.C. acknowledge support by the National Science Foundation under grant no. DMR-2118020.

References

1. Rozier, P. & Tarascon, J. M. Review—Li-Rich Layered Oxide Cathodes for Next-Generation Li-Ion Batteries: Chances and Challenges. *J. Electrochem. Soc.* **162**, A2490 (2015).
2. Li, M. *et al.* Cationic and Anionic Redox in Lithium-ion based Batteries.
3. Zhang, M. *et al.* Pushing the limit of 3d transition metal-based layered oxides that use both cation and anion redox for energy storage. *Nat Rev Mater* **7**, 522–540 (2022).
4. Li, B. & Xia, D. Anionic Redox in Rechargeable Lithium Batteries. *Advanced Materials* **29**, 1701054 (2017).
5. Assat, G. & Tarascon, J.-M. Fundamental understanding and practical challenges of anionic redox activity in li-ion batteries. *Nature Energy* **3**, 373–386 (2018).
6. Dh, S. *et al.* The structural and chemical origin of the oxygen redox activity in layered and cation-disordered Li-excess cathode materials. *Nature chemistry* **8**, (2016).
7. Saha, S. *et al.* Exploring the bottlenecks of anionic redox in Li-rich layered sulfides. *Nature Energy* **4**, 977–987 (2019).
8. Eum, D. *et al.* Voltage decay and redox asymmetry mitigation by reversible cation migration in lithium-rich layered oxide electrodes. *Nature Materials* **19**, 419–427 (2020).
9. Li, B. *et al.* Lithium Rich Layered Sulfides As a New-Type Cathode for Lithium Ion Batteries. *Meet. Abstr.* **MA2016-03**, 150 (2016).
10. Flamary-Mespoulie, F. *et al.* Lithium-rich layered titanium sulfides: Cobalt- and Nickel-free high capacity cathode materials for lithium-ion batteries. *Energy Storage Materials* **26**, 213–222 (2020).
11. Shadike, Z. *et al.* Antisite occupation induced single anionic redox chemistry and structural stabilization of layered sodium chromium sulfide. *Nat Commun* **8**, 566 (2017).
12. Leube, B. T. *et al.* Activation of anionic redox in d0 transition metal chalcogenides by anion doping. *Nat Commun* **12**, 5485 (2021).

13. Delmas, C., Fouassier, C. & Hagenmuller, P. Structural classification and properties of the layered oxides. *Physica B+C* **99**, 81–85 (1980).

14. Hansen, C. J. *et al.* Multielectron, Cation and Anion Redox in Lithium-Rich Iron Sulfide Cathodes. *J. Am. Chem. Soc.* **142**, 6737–6749 (2020).

15. Fleet, M. E., Harmer, S. L., Liu, X. & Nesbitt, H. W. Polarized X-ray absorption spectroscopy and XPS of TiS3: S K- and Ti L-edge XANES and S and Ti 2p XPS. *Surface Science* **584**, 133–145 (2005).

16. Zhang, L. *et al.* Tracking the Chemical and Structural Evolution of the TiS2 Electrode in the Lithium-Ion Cell Using Operando X-ray Absorption Spectroscopy. *Nano Lett.* **18**, 4506–4515 (2018).

17. Gilbert, P. *et al.* Multiple Scattering Calculations of Bonding and X-ray Absorption Spectroscopy of Manganese Oxides. *J. Phys. Chem. A* **107**, (2010).

18. Radin, M. D. & Van der Ven, A. Stability of Prismatic and Octahedral Coordination in Layered Oxides and Sulfides Intercalated with Alkali and Alkaline-Earth Metals. *Chem. Mater.* **28**, 7898–7904 (2016).

19. Tarascon, J. M., DiSalvo, F. J., Eibschutz, M., Murphy, D. W. & Waszczak, J. V. Preparation and chemical and physical properties of the new layered phases Li x Ti 1 − y M y S 2 with M = V , C r , o r F e. *Phys. Rev. B* **28**, 6397–6406 (1983).

20. Ravel, B. & Newville, M. ATHENA, ARTEMIS, HEPHAESTUS: data analysis for X-ray absorption spectroscopy using IFEFFIT. *J Synchrotron Rad* **12**, 537–541 (2005).

21. Kresse, G. & Furthmüller, J. Efficiency of ab-initio total energy calculations for metals and semiconductors using a plane-wave basis set. *Computational Materials Science* **6**, 15–50 (1996).

22. Kresse, G. & Joubert, D. From ultrasoft pseudopotentials to the projector augmented-wave method. *Phys. Rev. B* **59**, 1758–1775 (1999).

23. Blöchl, P. E. Projector augmented-wave method. *Phys. Rev. B* **50**, 17953–17979 (1994).

24. Perdew, J. P., Burke, K. & Ernzerhof, M. Generalized Gradient Approximation Made Simple. *Phys. Rev. Lett.* **77**, 3865–3868 (1996).

25. Dudarev, S. L., Botton, G. A., Savrasov, S. Y., Humphreys, C. J. & Sutton, A. P. Electron-energy-loss spectra and the structural stability of nickel oxide: An LSDA+U study. *Phys. Rev. B* **57**, 1505–1509 (1998).